RESEARCH ARTICLE

ADVANCED OPTICAL MATERIALS
www.advopticalmat.de

Transition-Metal Azo Schiff Base Complexes: Nonlinear Optics Across Solutions, Thin Films and Nanocomposites

Karolina Waszkowska, Mark Busch, Siham Slassi, Amina Amine, Abdelkrim El-Ghayoury,* Janusz Strzelecki, Anna Zawadzka, Andriy V. Kityk,* Patrick Huber,* and Bouchta Sahraoui**

This paper investigates the nonlinear optical (NLO) properties of azo-based Schiff base ligand and its corresponding complexes incorporating Cu(II) and Zn(II) metal cations, designed upon the previous synthesis work. Both 2nd and 3rd order NLO properties are examined, with a particular focus on their potential for optoelectronic and photonic applications. The Z-scan technique is employed to analyze NLO refraction and NLO absorption in solution. All samples exhibit positive NLO phenomena, with $Zn(L)_2$ showing the highest values ($\chi^{(3)} = 27.95 \times 10^{-22}$ m^2 V^{-2}, $\gamma = 54.44 \times 10^{-47}$ m^5 V^{-2}), attributed to enhanced ligand-to-metal charge transfer (LMCT). Additionally, thin films deposited via the spin coating method undergo 3rd order NLO analysis through the Maker fringe technique. THG analysis further confirms superior 3rd order NLO performance in $Zn(L)_2$, exceeding several benchmark transition-metal complexes. 2nd order NLO properties are also explored in hybrid nanocomposites designed from $Zn(L)_2$ embedded in nanoporous pSiO$_2$ membrane. This structure exhibits anisotropic SHG behavior, with $\chi^{(2)} = 0.11$ pm V^{-1} under s-p polarization, suggesting polarization confinement within nanochannels. The results clearly demonstrate that transition-metal azo Schiff base complexes, particularly $Zn(L)_2$, exhibit strong NLO responses, positioning them as potential candidates for applications in all-optical switching and frequency conversion.

1. Introduction

Nonlinear optics (NLO) refers to the study of how materials respond to intense electromagnetic fields, typically from lasers, resulting in phenomena such as self-focusing, frequency doubling, and multi-photon absorption.[1–6] NLO materials are specifically designed for their ability to manipulate light in ways that go beyond the capabilities of conventional optics. Among the organic materials, transition-metal complexes, particularly those based on Cu(II) and Zn(II), have attracted significant interest in the NLO field due to their remarkable electronic and structural versatility.[7–10] Transition metals possess *d*-electrons that contribute to enhanced electronic polarization, making them ideal candidates for generating strong NLO responses.[11,12] When these metal centers are incorporated into coordination frameworks such as azo Schiff base ligands, the resulting complexes exhibit a rich interplay between the metal's

K. Waszkowska, B. Sahraoui
Univ Angers
LPHIA
SFR MATRIX
Angers F-49000, France
E-mail: karolina.waszkowska@univ-angers.fr; bouchta.sahraoui@univ-angers.fr

M. Busch, P. Huber
Institute for Materials and X-ray Physics
Hamburg University of Technology
21073 Hamburg, Germany
E-mail: patrick.huber@tuhh.de

M. Busch, P. Huber
Centre for X-ray and Nano Science
Deutsches Elektronen-Synchrotron DESY
22607 Hamburg, Germany

S. Slassi
Laboratory of Engineering and Materials (LIMAT)
Faculty of Sciences Ben M'Sik
Hassan II University of Casablanca
B. P 7955, Casablanca 20670, Morocco

S. Slassi, A. Amine
LCBAE
Equipe Chimie Moléculaire et Molécules Bioactives URL-CNRST N° 13
Université Moulay Ismail
Faculté des Sciences
Meknès 11201, Morocco

A. El-Ghayoury
Univ Angers
CNRS
MOLTECH-ANJOU
SFR MATRIX
Angers F-49000, France
E-mail: abdelkrim.elghayoury@univ-angers.fr

The ORCID identification number(s) for the author(s) of this article can be found under https://doi.org/10.1002/adom.202500975

DOI: 10.1002/adom.202500975

electronic structure and the organic ligands, resulting in enhanced NLO behavior.[13]

Azo Schiff base complexes, characterized by the presence of azo (N═N) and Schiff base (C═N) functional groups, have been extensively studied and have found applications across various fields due to their unique properties and reactivity. Firstly, these compounds play a significant role in pharmaceutical and biological industries, primarily due to their antibacterial and antifungal properties.[14–17] Moreover, they are useful in the development of new smart materials, for example, through incorporation into polymer matrices or through the exploitation of their colorimetric properties.[18–20] Furthermore, these groups facilitate extensive π-conjugation throughout the molecule, enabling efficient charge transfer under light exposure.[21,22] The interaction between the metal center and the delocalized electron system of the ligand further amplifies NLO effects, positioning azo Schiff base complexes as promising candidates for advanced applications such as data storage, optical switching, and signal processing.[23–25]

In recent years, (nano/meso)porous membranes and films have emerged as valuable and versatile tools in diverse fields, including sensing, catalysis, filtration, and photonics.[26–30] Their key advantage lies in the precisely controlled nanometer-scale pore structures, which allow for fine-tuning of material properties that can be used for specific applications.[31–35] One of the most interesting developments is their use in NLO, where they offer superior performance compared to traditional bulk materials and thin films.[36,37] What sets nanoporous membranes apart is their precisely engineered pore architecture, which can be tailored in terms of pore size, distribution, and overall porosity. This opens up a wide range of possibilities in material design. In NLO applications, these membranes serve as an ideal host to incorporate materials like photonic crystals, organic chromophores, metal complexes, or quantum dots, all known for their strong NLO properties.[38–40] A major advantage of nanoporous membranes in NLO is their ability to bypass the strict phase matching conditions, typically required in conventional second and third harmonic generation (SHG and THG, respectively) materials.[41] This makes them particularly studied for compact and flexible photonic devices where traditional phase matching is impractical. Another importance is the mechanical and thermal stability of nanoporous membranes.[42–45] Unlike organic thin films, which can degrade under high temperatures or intense light exposure, nanoporous membranes provide a strong framework that protects the incorporated NLO materials. This stability is crucial for high-power laser applications and environments where durability and long-term performance are critical. Consequently, these hybrid systems provide reliable, repeatable NLO responses, critical for applications like optical limiting, data storage, and frequency conversion. Despite the promising optical characteristics of transition-metal azo Schiff base complexes and the increasing interest in nanoporous hybrid systems, there remains a lack of the systematic studies investigating how coordination geometry and guest-host interactions influence 2nd and 3rd order NLO responses in such platforms. This gap motivates the present work.

This study is a continuation of our previous work, which focused on the synthesis, crystal structure analysis, photoisomerization studies, and antibacterial activity of Cu(II) and Zn(II) complexes with an azo-based Schiff base ligand.[46] However, the NLO properties of these complexes, particularly embedded in functional nanoporous membranes, remain unexplored. The present work addresses this gap by systematically investigating the NLO responses of these transition-metal complexes across three complementary regimes. Firstly, we investigated NLO refraction and NLO absorption via the Z-scan technique in solution. Next, we explored THG in guest-host thin films. Finally, we examined SHG in hybrid nanocomposites. This multi-scale approach enables a detailed investigation of the interplay between coordination geometry, electronic structure, and host environment in controlling the optical nonlinearity. Moreover, the strong π-conjugation and efficient intramolecular charge transfer, make them excellent candidates for NLO applications. Our findings demonstrate the strong potential of azo Schiff base complexes in tailoring NLO properties, especially within porous platforms, offering a tunable materials for advanced photonic device development.

2. Results and Discussion

2.1. Samples Preparation

2.1.1. Synthesis

The chemical structures of the azo Schiff base ligand($C_{17}H_{19}N_3O$), namely L, prepared via the condensation of 2-hydroxy-5-(o-tolyldiazenyl)benzaldehyde and propylamine; copper(II) complex ($C_{34}H_{36}CuN_6O_2$), namely $Cu(L)_2$, and zinc(II) complex ($C_{34}H_{36}ZnN_6O_2$), namely $Zn(L)_2$, investigated in this study, are presented in **Figure 1**. As previously reported,[46] L was characterized using infrared (IR) and NMR spectroscopies, mass spectrometry, and X-ray diffraction, confirming its ability to function as a bidentate chelate through coordination via the deprotonated phenolic oxygen and azomethine nitrogen. Crystallization of the transition-metal complexes revealed that the copper complex, $Cu(L)_2$, adopts a square planar geometry, while the zinc complex, $Zn(L)_2$, exhibits a distorted tetrahedral arrangement, crystallizing in triclinic and orthorhombic systems with space groups P−1 and $Pca2_1$, respectively.[46]

J. Strzelecki
Department of Biophysics
Institute of Physics
Faculty of Physics
Astronomy and Informatics
Nicolaus Copernicus University in Toruń
Grudziadzka 5, Toruń 87-100, Poland
A. Zawadzka
Institute of Physics
Faculty of Physics
Astronomy and Informatics
Nicolaus Copernicus University in Toruń
Grudziadzka 5, Toruń 87-100, Poland
A. Zawadzka
Centre for Modern Interdisciplinary Technologies
Nicolaus Copernicus University in Toruń
Wilenska 4, Toruń 87-100, Poland
A. V. Kityk
Faculty of Electrical Engineering
Częstochowa University of Technology
Al. Armii Krajowej 17, Częstochowa 42-200, Poland
E-mail: andriy.kityk@pcz.pl

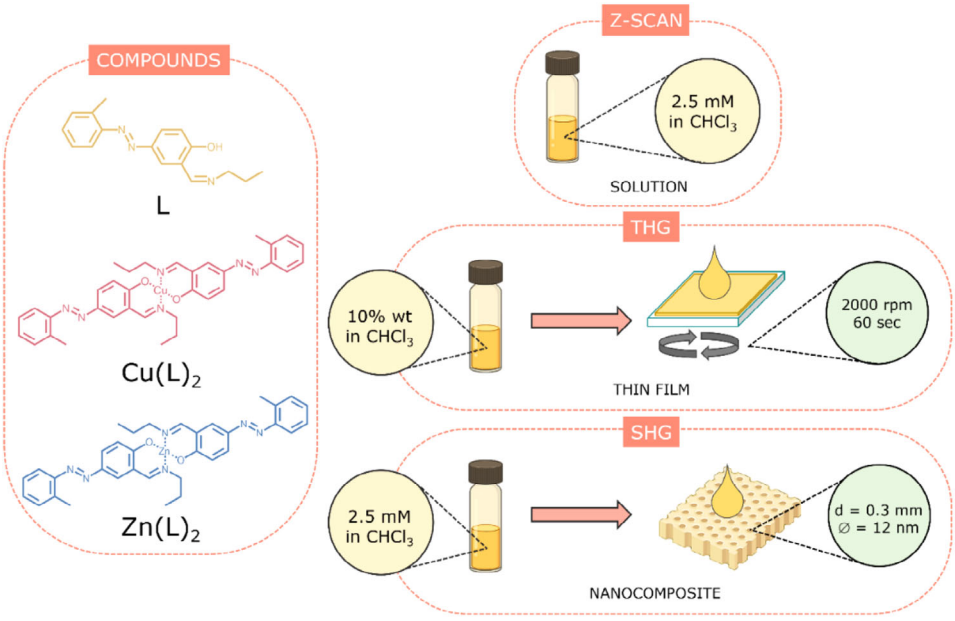

Figure 1. Schematic representation of L, $Cu(L)_2$, and $Zn(L)_2$ preparation for NLO research.

2.1.2. Membranes

Porous silica ($pSiO_2$) membranes are prepared by thermally oxidizing porous silicon (pSi) membranes in air at 900 °C. The pSi is synthesized through an anodic etching of p^+ boron-doped, single-crystalline (100) Si wafers with a resistivity of 0.01–0.02 Ω cm. A current density of 12 mA cm^{-2} is applied for the Si etching in a 2:3 mixture of hydrofluoric acid (48%) and ethanol. Afterward, a free-standing pSi membrane is obtained by detaching the pSi layer from the remaining bulk silicon by an electropolishing step. The resulting nanoporous $pSiO_2$ membrane is characterized by high transparency, with a thickness of 0.35 mm. Its pore diameter of 12 nm was determined by employing a nitrogen sorption isotherm analysis with an NLDFT model (Quantachrome Instruments).

2.1.3. Z-Scan Solutions

In the Z-scan technique, the studied compounds were dissolved in 1 mL of chloroform ($CHCl_3$) to form 2.5 mM solutions. Each solution was prepared under controlled conditions to ensure uniform concentration and homogeneity, with magnetic stirring used to facilitate even mixing.

2.1.4. Thin Films

For the THG experiment, poly(methyl methacrylate) (PMMA) with an average molecular weight of ≈120 000 (determined by GPC, Sigma-Aldrich) was dissolved in $CHCl_3$ to a concentration of 50 mg mL^{-1} (5%). Each of the three compounds was added to this polymer solution at a concentration of 10% by weight relative to the dry polymer mass. The resulting solutions were then applied onto isopropanol vapor-cleaned glass substrates (BK7) and spin-coated at 2000 rpm for 60 s using a vacuum-free spin-coater (Ossila) to create uniform thin films.

2.1.5. Nanocomposites

The SHG experiment was conducted on a hybrid nanostructure composed of a $pSiO_2$ nanoporous membrane and the studied transition-metal complex $Zn(L)_2$. A 2.5 mM solution of the complex/$CHCl_3$ was introduced into the membrane and left for 3 h to allow the solvent to evaporate. The sample preparation at all stages is schematically illustrated in Figure 1.

2.2. Thin Films Characterization

Initially, we measured the thickness of the guest-host films using a profilometer, revealing a thickness ranging from 800 to 1300 nm. Following this, we examined the morphology of the studied thin films. These observations are crucial for understanding how the physical characteristics of the films influence their performance in NLO investigations. The optical microscope images, presented in Figures S1a–S3a (Supporting Information), offer a remarkable visual insight into the analyzed layers. These images reveal a high degree of homogeneity across thin films, with only a few minor defects. However, these imperfections are not significant enough to impact THG studies. In fact, we confidently affirm that the investigated films exhibit excellent optical quality for NLO research. With their homogeneous structure and minimal imperfections, these films are well-suited for advancing THG studies, furthering our understanding of light-matter interactions.

In our study of NLO materials, the refractive index plays a key role, slightly yet influencing optical behaviors like THG. Using the precision of ellipsometry, we measured changes in the linear refractive index, extracting key parameters essential for understanding these NLO processes. While the deviations from the standard values for bulk PMMA are small in our guest-host films,[47] their impact is anything but minor. Even slight shifts in the refractive index can alter the efficiency of harmonic generation, making these measurements crucial for accurately calculating NLO susceptibility values with accuracy (see Supporting Information). Our findings, including refractive index values at the laser's output wavelength of 1064 nm and the THG wavelength of 355 nm, are illustrated in Figures S1b–S3b (Supporting Information) and detailed in Table S1 (Supporting Information). Moreover, the calculated permittivity values (ε) show real parts (ε') between 2.22 and 2.38 and low imaginary parts (ε″), indicating low optical losses at 1064 and 355 nm for all the samples (Table S1, Supporting Information). Slight variations in ε' correlate with metal coordination effects, with $Zn(L)_2$ exhibiting the highest ε' at 355 nm, suggesting an enhanced THG response.

To gain a deeper understanding of the surface characteristics, we conducted an in-depth analysis of the thin films' topography at the nanometer scale using Atomic Force Microscopy (AFM). The detailed results, illustrated in Figures S4–S6 (Supporting Information), confirm that the films are mainly homogeneous, with no major defects detected. The average roughness (R_A) and root mean square (RMS; R_Q) over the areas 3 × 3 μm^2 were calculated from the AFM data, while Figure S7 (Supporting Information) provides a clear height distribution density of the analyzed layers. A summary of all the parameters determined in this section can be found in Table S1 (Supporting Information). These morphological characteristics are not only crucial for ensuring optical quality but also correlate with the NLO response. The $Zn(L)_2$ guest-host film, which exhibits the lowest RMS roughness (0.08 nm), also shows the highest dielectric constant at 355 nm (ε' = 2.375) and should yield the strongest THG signal. In contrast, the $Cu(L)_2$ film, with a higher RMS value (0.39 nm), demonstrates a higher extinction coefficient (k = 0.027 at 355 nm), possibly due to increased surface-induced scattering, which may reduce THG efficiency. The L ligand film presents an intermediate case, which has a slightly higher RMS roughness (0.10 nm) than $Zn(L)_2$ and a moderate ε' value of 2.280 at 355 nm. Correspondingly, its THG response should be weaker than $Zn(L)_2$ but still detectable. These trends suggest that smoother films with fewer nanometric surface features allow more coherent light-matter interaction and stronger 3rd order NLO responses. Therefore, while all films are optically suitable, minor roughness differences correlate with measurable variations in THG performance, supporting the role of (nano)structural morphology in NLO behavior.

2.3. Absorption and Emission Spectroscopy

The normalized UV–vis absorption spectra of the guest-host films were recorded over the range of 300–1100 nm (**Figure 2**), revealing shifts that highlight interaction between the ligand and its transition-metal complexes. For clarity, the absorption spectra in Figure 2 are cut off at 600 nm, as the thin films are optically transparent beyond this wavelength (Figure S8, Supporting

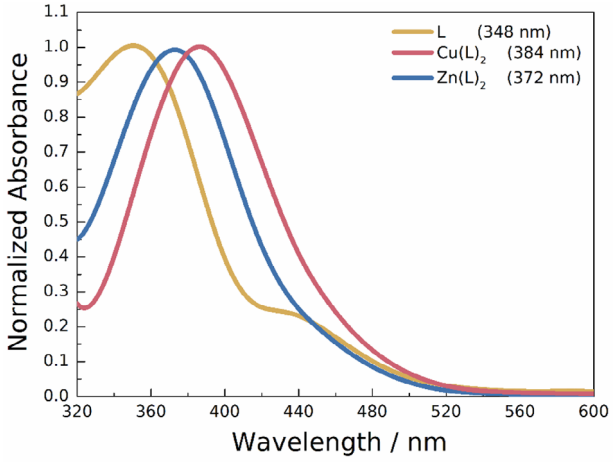

Figure 2. Normalized absorption spectra of L, $Cu(L)_2$, and $Zn(L)_2$ guest-host films embedded in PMMA.

Information). The ligand L itself displayed a sharp absorption peak at 348 nm, while coordination with metals led to noticeable red shifts. The $Zn(L)_2$ complex exhibited a peak at 372 nm, and the $Cu(L)_2$ complex showed an even further shift, with its peak appearing at 384 nm. These shifts suggest strong coordination between the ligand and metal centers, likely influenced by ligand-to-metal charge transfer transitions (LMCT).[46] Although our spectra extend from 300 to 1100 nm, it is important to note that transitions below 300 nm (not shown due to strong absorption of the BK7 glass substrate) correspond to high-energy π–π^* and n–π^* transitions, primarily associated with the aromatic rings and chromophore groups in the ligand structure.[46] These high-energy transitions, though beyond our measured range, are important for understanding the full electronic behavior of the system. Notably, we observed significant absorbance at 355 nm, which corresponds to the THG wavelength. This suggests that, in a THG experiment, part of the generated signal may be absorbed by the sample, potentially affecting the overall efficiency of the process. To quantify this effect, we calculated the linear absorption coefficient specifically at 355 nm, with the results presented in Table S2 (Supporting Information).

Using our knowledge of the absorption maxima, we conducted photoluminescence (PL) studies by exciting the samples at their respective absorption wavelengths. The resulting emission spectra, shown in Figures S9a–S11a (Supporting Information), reveals that all the samples emit within the violet range of the spectrum. For the $Cu(L)_2$ complex, two emission peaks were identified – one more intense at 435 nm and a second, weaker peak at 415 nm. This dual emission behavior is most likely due to distinct electronic transitions within the ligand-metal coordination system, potentially involving ligand-centered (π–π^*) and metal-perturbed transitions, rather than any interaction with PMMA, which is known to be optically transparent. The red shift observed in the absorption spectra of the $Zn(L)_2$ and $Cu(L)_2$ complexes compared to the free ligand L suggests that coordination to the transition-metals modifies the electronic structure, enhancing charge transfer interactions. This shift in energy levels is reflected in the observed photoluminescence, with the $Cu(L)_2$ complex exhibiting a more complex emission profile due to its unique

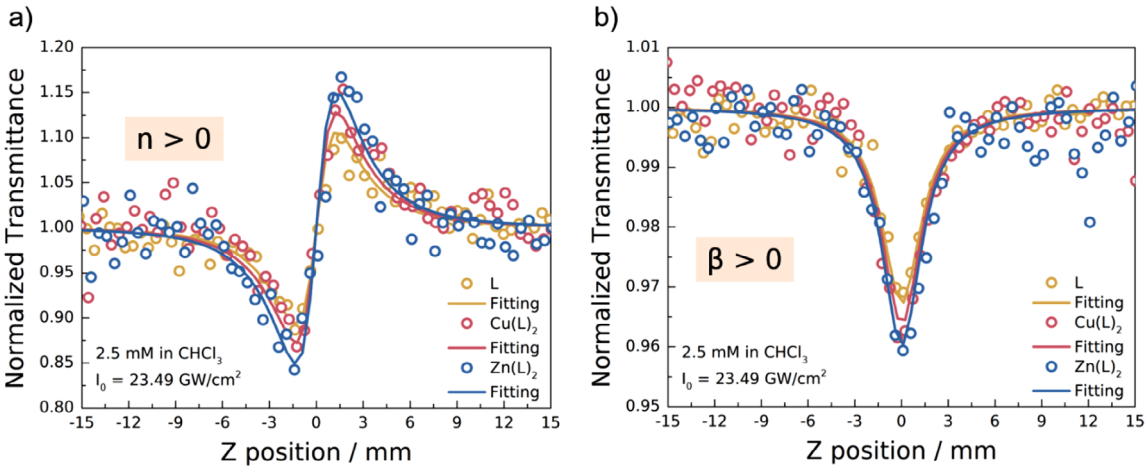

Figure 3. CA a) and OA b) Z-scan curves for L, $Cu(L)_2$, and $Zn(L)_2$ dissolved in $CHCl_3$ with concentration 2.5 mM at 532 nm and 23.49 GW cm^{-2} laser density.

electronic environment. Additionally, we recorded PL intensity maps as functions of excitation and emission wavelengths, as presented in Figures S9b–S11b (Supporting Information). These maps, analyzed using FluoroEssence software, reveal shifts in the excitation maxima that corresponds to the observed emission peaks. The 3D PL maps enabled precise determination of the wavelengths where the PL intensity reached maximum, as summarized in Table S2 (Supporting Information). We also measured the PL lifetime (Figure S12, Supporting Information) and fitted the decay data using a double-exponential function.[48] The resulting decay times, τ_{1a} and τ_{1b}, showed minimal variation across the samples (Table S2, Supporting Information), and are primarily associated with π-π^* transitions within the ligand structure. The average decay time T, calculated from τ_1 and τ_1, and their respective amplitudes, reflects the combined contribution of these transitions and indicates that coordination with metal ions slightly influences the overall decay dynamics. The 2.60 ns lifetime observed for the free ligand L is attributed to its azo Schiff base structure, which chelates the metal via phenolic oxygen and azomethine nitrogen, stabilizing the excited state without significant quenching. The 2.61 ns lifetime observed for $Zn(L)_2$ is comparable to that of the free ligand, as Zn(II) (a d_{10} metal) does not affect the excited state due to absence of unpaired electrons, resulting in minimal quenching. In contrast, the 1.83 ns lifetime observed for $Cu(L)_2$ is shorter, reflecting the quenching effects of the Cu(II) metal center, which, as a d_9 metal, promotes nonradiative decay. This interplay results in the observed emission characteristics. The observed characteristics, driven by π–π^* transitions and ligand-metal interactions, further enhance their potential for NLO studies, where controlled emission and absorption properties are important.

2.4. Nonlinear Refraction and Nonlinear Absorption

Our research on 3rd order NLO phenomena has been significantly advanced by the Z-scan method, a powerful technique that enables simultaneous determination of both electronic and molecular contributions to the 3rd order NLO susceptibility, $\chi^{(3)}$. In this study, we used 2.5 mM solutions of the samples dissolved in $CHCl_3$, as illustrated in Figure 1. $CHCl_3$, known for its high NLO refractive index,[49] played an important role in our calculations (Figure S13, Supporting Information). To accurately assess the $\chi^{(3)}$ of our complex, we carefully accounted for the solvent's contribution by subtracting the NLO refractive index, n_2, of $CHCl_3$ from the measured n_2 of the solution.[50] This procedure allowed us to isolate and calculate $\chi^{(3)}$ specifically for the complex.

The graphical representation of the Z-scan measurements for both the CA and OA configurations is presented in **Figure 3**, while the corresponding calculated parameters are summarized in **Table 1**. All three samples – L, $Cu(L)_2$, and $Zn(L)_2$ – exhibit a positive NLO refractive index ($n_2 > 0$), indicative of the self-focusing effect. Notably, this effect is more pronounced in the metal complexes compared to the free ligand, highlighting the enhanced NLO properties associated with metal coordination. The stronger self-focusing effect observed in the Zn(II) complex relative to the Cu(II) complex can be attributed to the nature of their d orbitals. In Zn(II), the d orbitals are fully filled (d_{10} configuration), allowing for more effective orbital overlap and stronger electronic interactions. This results in better

Table 1. Values of NLO refractive index (n_2), NLO absorption coefficient (β), NLO cross section parameter (σ), real, imaginary and total value of 3rd order NLO susceptibility ($\chi^{(3)}$), 2nd hyperpolarizability (γ) and figure-of-merit (FOM) of investigated L, $Cu(L)_2$, and $Zn(L)_2$ samples at 532 nm.

	L	$Cu(L)_2$	$Zn(L)_2$	$CHCl_3$
$n_2 \times 10^{-19}$ m^2 W^{-1}	2.69	3.23	3.81	1.65
$\beta \times 10^{-13}$ m W^{-1}	0.56	0.62	0.68	N/A
$\sigma \times 10^{-56}$ m^4 s	1.39	1.54	1.69	N/A
$Re(\chi^{(3)}) \times 10^{-22}$ m^2 V^{-2}	19.73	23.69	27.95	10.4
$Im(\chi^{(3)}) \times 10^{-22}$ m^2 V^{-2}	0.17	0.19	0.21	N/A
$\chi^{(3)} \times 10^{-22}$ m^2 V^{-2}	19.73	23.69	27.95	10.4
$\gamma \times 10^{-47}$ m^5 V^{-2}	38.43	46.15	54.44	3.28
FOM	1.81	1.96	2.11	N/A

stabilization of excited states, leading to enhanced NLO responses. In contrast, the d orbitals in Cu(II) (d_9 configuration) are partially filled, resulting in different electronic behavior that contributes to a comparatively weaker NLO response. Furthermore, all samples exhibited positive NLO absorption ($\beta > 0$) at 532 nm, corresponding to 2-photon absorption processes (2PA) originating from 266 nm. The trend in 2PA values is significant, with $Zn(L)_2$ demonstrating the highest 2PA, followed by $Cu(L)_2$ and then the ligand L. This behavior can be attributed to the enhanced electronic interactions facilitated by the metal cations during the π–π^* transitions occurring at this critical wavelength.

Using the data collected from these measurements, we calculated values of the 3rd order NLO susceptibility, and 2nd hyperpolarizability (see Supporting Information), which are detailed in Table 1. The estimated error in these calculations is ≈ 0.5%. The total value of $\chi^{(3)}$ was derived from the calculated real and imaginary components, revealing that NLO effects are significantly enhanced in the metal complexes compared to the free ligand. At the laser wavelength of 532 nm, the imaginary part of the $\chi^{(3)}$ contributes minimally, indicating that the NLO effects are primarily controlled by the real component. Notably, the Zn(II) complex exhibits stronger nonlinearity, attributed to its higher chemical activity and stronger electronic interactions resulting from its filled d orbitals. To assess the suitability of these azo Schiff-base complexes for nonlinear photonic switching, we also calculated the figure-of-merit (FOM) defined as FOM $= 2n_2/\lambda\beta$, where λ is the laser wavelength.[51] This FOM reflects the balance between NLO refraction (desirable) and NLO absorption (undesirable) in the materials. The resulting FOM values were 2.11 for Zn(II) complex $Zn(L)_2$, 1.96 for Cu(II) complex $Cu(L)_2$, and 1.81 for the ligand L, indicating that all samples fall within a favorable regime, where FOM > 1,[51] for optical switching applications. These values reinforce the potential of these transition-metal complexes in all-optical signal modulation platforms.

2.5. Third Harmonic Generation

Moreover, the exploration of 3rd order NLO effects through THG phenomena was conducted on thin films using the Maker fringe method in transmission mode. This experimental setup involved s-p polarized configurations of laser light, as the observed phenomena are independent of laser polarization. Although the intensity of the THG signal tends to rise with increasing sample thickness due to the increased optical length, $\chi^{(3)}$ values themselves are unaffected by sample thickness, as it is an intrinsic property of the material.[52] The visual representation of these studies is presented in **Figure 4**. The 3rd order NLO susceptibility values were determined from the Maker fringes, using two models (see Supporting Information), and the calculated dataset is presented in **Table 2**. The error associated with these calculations has been estimated to be ≈ 0.1%.

It is crucial to note that THG contributes only electronically to the 3rd order NLO susceptibility. By employing the more precise model proposed by Reintjes, no significant improvement was observed in calculations compared to the conventional comparative model (Figure S14, Supporting Information). Moreover, the obtained THG response for the samples is significantly stronger than that of the reference material and the BK7 glass substrate, as illustrated in Figure S15 (Supporting Information). These studies confirm that the $Zn(L)_2$ complex exhibits the most pronounced THG response due to its inherent chemical activity and strong electronic interactions, primarily facilitated by the enhanced LMCT processes. This charge transfer occurs between the filled *d* orbitals in the Zn(II), resulting in improved electronic coupling and stabilization of excited states. The data clearly affirm that the studied azo Schiff base complexes are promising candidates for applications based on 3rd order NLO effects, with a particular emphasis on the $Zn(L)_2$ complex.

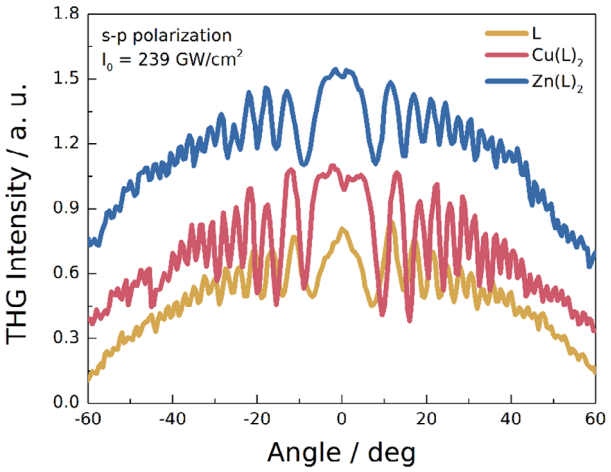

Figure 4. THG intensities versus rotation angle in s-p polarized laser beam of L, $Cu(L)_2$, and $Zn(L)_2$ guest-host thin films embedded in PMMA at 1064 nm and 239 GW cm^{-2} laser density.

B. Kulyk et al. investigated the NLO properties of functionalized azo-based iminopyridine rhenium complexes, namely $L1Re(CO)_3Cl$ and $L2Re(CO)_3Cl$.[53] These complexes are characterized by the presence of electron-donating dimethylamino groups or electron-withdrawing nitro groups attached to the azo-based iminopyridine ligand. Notably, $L1Re(CO)_3Cl$ exhibits a significantly higher $\chi^{(3)}$ value compared to azo Schiff base complexes, an effect attributed to the rhenium metal center, the electronic properties of the iminopyridine ligand, and the donor nature of the dimethylamino group, which enhances electron density. Additionally, $L1Re(CO)_3Cl$ displays a relatively high γ value, suggesting that the presence of an electron-donating dimethylamino group enhances the NLO response, whereas the nitro group in $L2Re(CO)_3Cl$ reduces γ value due to its electron-withdrawing nature. However, among the investigated systems, the $Zn(L)_2$ complex exhibits the highest γ value, likely due to increased geometric distortion and strong metal-ligand interactions. The azo group in Schiff base ligands promotes electronic delocalization and polarizability, particularly when coordinated to metal centers such as Cu(II) and Zn(II), where strong metal-ligand interactions significantly influence the overall electronic structure. The bidentate coordination further enhances the polarization of these complexes.

S. Taboukhat et al. studied the NLO effects of Ru- and Fe-based transition metal organometallic complexes (1–4).[54] These complexes, coordinated with phosphines, aryl groups, or

Table 2. 3rd order NLO susceptibility ($\chi^{(3)}$) and 2nd hyperpolarizability (γ) values for the L, $Cu(L)_2$ and $Zn(L)_2$ guest-host thin films in s-p polarization calculated by comparative and Reintjes models at 1064 nm, compared with other reported complexes.

Complex/PMMA	Model	$\chi^{(3)} \times 10^{-22}$ m^2 V^{-2}	$\gamma \times 10^{-47}$ m^5 V^{-2}	Refs.
L[a]	Comparative	10.79	2.37	This work
	Reintjes	11.21	2.48	This work
$Cu(L)_2$[a]	Comparative	11.80	6.52	This work
	Reintjes	12.56	6.94	This work
$Zn(L)_2$[a]	Comparative	21.76	10.71	This work
	Reintjes	23.34	11.43	This work
L1$Re(CO)_3Cl$[b]	Comparative	30.4	2.59	[53]
L2$Re(CO)_3Cl$[b]	Comparative	8.19	0.70	[53]
1 (Fe)[c]	Comparative	61	5.55	[54]
2 (Ru)[c]	Comparative	35	3.22	[54]
3 (Ru)[c]	Comparative	25	2.26	[54]
4 (Ru)[c]	Comparative	27	2.44	[54]
1 (Cu)[d]	Comparative	8.84	N/A	[55]
2 (Co)[d]	Comparative	25.55	N/A	[55]
3 (Cd)[d]	Comparative	14.79	N/A	[55]
4 (Hg)[d]	Comparative	13.25	N/A	[55]
5 (Mn)[d]	Comparative	15.45	N/A	[55]
6 (Zn)[d]	Comparative	40.34	N/A	[55]
L1[e]	Comparative	19.28	N/A	[56]
	Reintjes	19.71	N/A	[56]
C1 (Zn)[e]	Comparative	14.19	N/A	[56]
	Reintjes	14.75	N/A	[56]
C2 (Cu)[e]	Comparative	12.26	N/A	[56]
	Reintjes	14.06	N/A	[56]

[a] azo Schiff base complexes; [b] azo-based iminopyridine rhenium complexes; [c] transition metal organometallic complexes; [d] transition metal coordination complexes; [e] stilbene based iminopyridine complexes.

carbocyclic ligands, such as ferrocenylacetylene for Fe or bipyridine and triphenylphosphine for Ru, exhibit strong 3rd order NLO properties, primarily due to metal-ligand charge transfer (MLCT) and LMCT mechanisms. The Fe-based complex (1) demonstrates a remarkably high $\chi^{(3)}$ value of 61×10^{-22} m^2 V^{-2}, surpassing Schiff base complexes. This enhancement is attributed to the strong interaction between the ferrocenylacetylene ligand and the Fe center, which facilitates charge transfer interactions that amplify the NLO response. In comparison, Ru-based complexes exhibit $\chi^{(3)}$ values ranging from 25 to 35×10^{-22} m^2 V^{-2}, which, although lower than the Fe complex, remain significantly higher than Schiff base complexes. The Ru(II) centers in these complexes enable efficient metal-cantered charge transfer and MLCT interactions. Conversely, Schiff base complexes exhibit $\chi^{(3)}$ values between 10.79×10^{-22} m^2 V^{-2} (for L) and 21.76×10^{-22} m^2 V^{-2} (for $Zn(L)_2$), with $Zn(L)_2$ showing the highest value within this group. This observation suggests that the distorted tetrahedral geometry of Zn(II) enhances the NLO response. While transition metal organometallic complexes typically exhibit lower γ values, Ru-based complexes fall within the range of $2.26–3.22 \times 10^{-47}$ m^5 V^{-2}. Despite their MLCT-driven charge transfer effects, these complexes exhibit lower hyperpolarizability than azo Schiff base complexes. Among Schiff base complexes, $Zn(L)_2$ exhibits the most pronounced hyperpolarizability, likely due to the involvement of *d* orbitals, and the distorted tetrahedral geometry of Zn(II).

H. Belahlou et al. investigated THG phenomena in Cu(II), Co(II), Cd(II), Hg(II), Mn(II), and Zn(II) transition metal coordination complexes (1–6).[55] The Zn coordination complex (6) exhibits a $\chi^{(3)}$ value of 40.34×10^{-22} m^2 V^{-2}, significantly surpassing that of $Zn(L)_2$ (21.76×10^{-22} m^2 V^{-2}), making it the material with the strongest NLO response among the transition metal coordination complexes. This enhanced performance is attributed to its high polarization and a distinct coordination environment that affects the electronic structure. Similarly, $Cu(L)_2$ demonstrates a $\chi^{(3)}$ value of 11.80×10^{-22} m^2 V^{-2}, exceeding that of the Cu coordination complex (1) (8.84×10^{-22} m^2 V^{-2}), suggesting that Schiff base coordination enhances NLO properties compared to simple Cu(II) complexes. Among the transition metal coordination complexes, Co(II) (2) and Mn(II) (5) exhibit $\chi^{(3)}$ values of 25.55×10^{-22} and 15.45×10^{-22} m^2 V^{-2}, respectively, positioning them between Schiff base complexes and the highest-performing Zn(II) complex.

K. Waszkowska et al. conducted NLO studies on a stilbene-based iminopyridine ligand and its corresponding Zn(II) and Cu(I) complexes.[56] The stilbene-based ligand (L1) exhibits a $\chi^{(3)}$ value of 19.28×10^{-22} m^2 V^{-2}, surpassing the azo Schiff base ligand L (10.79×10^{-22} m^2 V^{-2}) but remaining lower than $Zn(L)_2$

(21.76×10^{-22} m^2 V^{-2}), which demonstrates the highest NLO response among azo Schiff base complexes. The stilbene-based iminopyridine complex features a π-conjugated trans-stilbene backbone that links a dimethylamino donor group to an iminopyridyl acceptor, forming a push-pull electronic structure that facilitates strong polarization and efficient electron density shifts. The Zn(II) complex (C1) in the stilbene-based series exhibits a $\chi^{(3)}$ value of 14.19×10^{-22} m^2 V^{-2}, exceeding L (10.79×10^{-22} m^2 V^{-2}) but falling below $Zn(L)_2$ (21.76×10^{-22} m^2 V^{-2}). Similarly, the Cu(I) complex (C2) demonstrates a $\chi^{(3)}$ value of 12.26×10^{-22} m^2 V^{-2}, exceeding L (10.79×10^{-22} m^2 V^{-2}) and $Cu(L)_2$ (11.80×10^{-22} m^2 V^{-2}) but significantly lower than $Zn(L)_2$. The metal centers in these complexes reveal additional electronic flexibility, the tetrahedral geometry in Zn(II) (C1) induces geometric distortion, altering electronic distribution and enhancing the NLO response. Similarly, the linear coordination of Cu(I) in C2 promotes charge transfer interactions that influence $\chi^{(3)}$. Azo Schiff base complexes, despite benefiting from metal coordination, experience limitations in electronic delocalization due to the electron-withdrawing nature of the azo group, resulting in less pronounced NLO compared to stilbene-based systems. The azo Schiff base ligand consists of an azo functional group attached to a Schiff base structure, which coordinates to a metal center. The electron-withdrawing effect of the azo group directs electron density toward the metal, leading to a more localized electronic structure. Consequently, azo Schiff base complexes tend to exhibit lower $\chi^{(3)}$ values due to their relatively rigid coordination geometries, which limit the flexibility necessary for strong NLO responses.

In comparison to other transition-metal complexes studied for their NLO properties, the azo Schiff base complexes, particularly $Zn(L)_2$ demonstrate superior performance. Various transition-metal complexes have been explored in literature, often exhibiting significant NLO effects. However, our results indicate that the 3rd order NLO susceptibility and 2nd hyperpolarizability values obtained from the $Zn(L)_2$ and $Cu(L)_2$ complexes exceed those reported for many similar systems. The enhanced electronic interactions facilitated by the *d* orbitals of the metal cations in our complexes contribute to more pronounced NLO effects. Additionally, the efficient LMCT processes observed in our complexes further distinguish them from others, leading to improved data storage capabilities.

To better evaluate the suitability of the studied transition-metal azo Schiff base complexes for 3rd order NLO applications, a FOM was calculated for each system, defined as FOM = $\chi^{(3)}/\alpha_{355}$.[57] The resulting FOM values were 3.42×10^{-27} m^3 V^{-2} for ligand L, 1.02×10^{-27} m^3 V^{-2} for Zn(II) complex $Zn(L)_2$, and 0.99×10^{-27} m^3 V^{-2} for Cu(II) complex $Cu(L)_2$. Despite $Zn(L)_2$ showing the highest 3rd order NLO susceptibility ($\chi^{(3)} = 23.34 \times 10^{-22}$ m^2 V^{-2}), its relatively high absorption coefficient at 355 nm ($\alpha_{355} = 22\,960$ cm^{-1}) results in a lower FOM compared to ligand L. On the other hand, ligand L, with the lowest absorption among the three systems ($\alpha_{355} = 3280$ cm^{-1}), yields the highest FOM, despite having a more modest NLO response. These results highlight the importance of high NLO susceptibility and transparency. While $Zn(L)_2$ remains a strong candidate due to its intense NLO response and excellent performance at infrared wavelengths, its linear optical losses in the UV region must be taken into account when designing THG-based devices, particularly operating near 355 nm. In contrast, ligand L shows a more favorable FOM at 355 nm, suggesting better performance in ultraviolet or visible-light based THG applications. The FOM calculated for these transition-metal azo Schiff base complexes, indicates an optimal balance between strong NLO susceptibility and moderate linear absorption at 355 nm. This balance is crucial for ultrafast all-optical switching, where materials must exhibit significant NLO refractive index changes with minimal loss to enable efficient modulation of signal without excessive heating or attenuation.

2.6. Second Harmonic Generation

Given the sensitivity of SHG method, which is restricted to materials without a center of the symmetry, the SHG response in the guest-host films was undetectable. Additionally, employing symmetry breaking techniques, such as the corona poling method,[58] no desired SHG effect was achieved in these materials (Figure S16, Supporting Information). Consequently, this section shifts its focus to SHG investigations provided in hybrid nanocomposites. Our preceding studies clearly illustrate that introducing a material into a nanoporous membrane can induce the SHG effect in materials that do not inherently exhibit this phenomenon.[36] Unlike previously reported SHG-active nanocomposites where active components already possessed 2nd order nonlinearity, the present system activates a non-SHG material via nanoscale confinement, offering a new route to induce symmetry breaking and anisotropy without external poling.

This section is devoted to the investigation of the SHG effect within a hybrid structure composed of a $pSiO_2$ membrane and the examined azo Schiff base compound $Zn(L)_2$, which was selected as a representative sample, namely $pSiO_2$:$Zn(L)_2$. Building upon our previous research on nanocomposites, we have established that the membrane itself does not generate the SHG signal (Figure S17, Supporting Information). The $pSiO_2$:$Zn(L)_2$ nanocomposite successfully demonstrated SHG recording, as shown in Figure S18 (Supporting Information). Notably, the dependence of the SHG signal on the applied polarization is clearly visible, indicating that these hybrid materials polarize laser light in the vertical direction, as evidenced by the amplified signal in the s-p polarization at 0°. The stronger intensity at 0° in s-p polarization is likely due to the electric field parallel to the surface working at full efficiency, without interference or complex molecular orientations. However, the polarization differences are significant (**Figure 5**), suggesting that this material behaves like an anisotropic medium, with different SHG response regardless of the polarization direction. This observation suggests that the SHG response is due to the dipole moments confined in nanochannels, rather than a surface effect. In the absence of phase matching, SHG signal is achieved within the nanopores filled with $Zn(L)_2$, due to the localized NLO polarization. The relatively short interaction path (0.35 nm) facilitates efficient energy transfer, while the localized interactions within the pores lead to average the effects of phase mismatch. This leads to the detection of a measurable SHG signal, as demonstrated below by a comparison of the $\chi^{(2)}$ values with those obtained from a standard reference material.

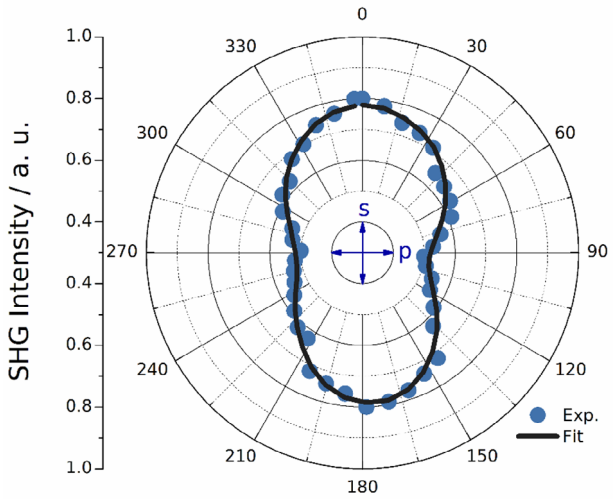

Figure 5. SHG polarization dependence at 0° of hybrid nanostructure $p\mathrm{SiO_2}$:$\mathrm{Zn(L)_2}$ at 1064 nm and 239 GW $\mathrm{cm^{-2}}$ laser density.

To quantify the 2nd order susceptibility, $\chi^{(2)}$, of the hybrid nanocomposite, we used a comparative approach with a standard reference material, specifically a 0.5 mm Y-cut quartz slab under identical optical conditions (Figure S19, Supporting Information).[59] This reference material was chosen due to its well-documented NLO properties and stable 2nd order susceptibility values, providing a reliable benchmark for assessing the performance of our nanocomposite.[60] It is important to note that the quartz slab is a highly anisotropic material, exhibiting a higher SHG intensity for s-p polarized light compared to p-p polarized light. As a result, the direct comparison procedure may amplify the calculated $\chi^{(2)}$ values for p-p polarization in the nanocomposite. To account for the anisotropic SHG response of the reference material, a polarization correction factor P (see Supporting Information), which is a ratio of the SHG intensity in p-p polarization to the SHG intensity in s-p polarization, was applied to the calculated $\chi^{(2)}$ and β values. In this approach, normalization accurately reflects the higher s-p response observed in the nanocomposite. The 2nd order susceptibility values for the $p\mathrm{SiO_2}$:$\mathrm{Zn(L)_2}$ nanocomposite, calculated for s-p polarization ($\chi^{(2)}$ = 0.11 pm $\mathrm{V^{-1}}$) and p-p polarization ($\chi^{(2)}$ = 0.02 pm $\mathrm{V^{-1}}$), highlight a significant difference in the NLO response between the polarization states. This difference is further reflected in the calculated 1st hyperpolarizability values, for s-p polarization ($\beta = 0.79 \times 10^{-40}$ $\mathrm{m^4\ V^{-1}}$) and p-p polarization ($\beta = 0.65 \times 10^{-40}$ $\mathrm{m^4\ V^{-1}}$). Moreover, the raw SHG intensity measurements for the nanocomposite show a stronger response for s-p polarization, suggesting that the underlying molecular anisotropy favors this configuration. These results underscore the anisotropic NLO behavior of the $p\mathrm{SiO_2}$:$\mathrm{Zn(L)_2}$ nanocomposite, which is influenced by both its molecular organization and the experimental conditions.

Compared to classical materials commonly used for SHG,[61–65] nanocomposites present distinct advantages. Unlike crystals, these materials do not require precise phase matching, which simplifies their application in practical optical systems, as the SHG originates only from the material introduced into the pores, and not from the host matrix, and the interaction is localized within discrete, nanoscale volumes. Additionally, for thin films, there is no need for techniques like corona poling, which can lead to degradation of organic materials under high temperatures. The stability of these hybrid nanocomposites, combined with their ability to generate SHG without the need for complex treatments, makes them promising candidates for photonic and optoelectronic device applications. Importantly, $\mathrm{Zn(L)_2}$ does not exhibit SHG in thin film form, but confinement within $p\mathrm{SiO_2}$ pores induces measurable 2nd order nonlinearity, highlighting a confinement-triggered activation mechanism not previously demonstrated for this class of materials. The current work demonstrates SHG activation in a system previously SHG-inactive, with polarization-dependent anisotropy confirming alignment driven by the pore geometry rather than external fields.

Nanoporous membranes possess unique properties that make them ideal for use in photonic and optoelectronic devices. For instance, their ability to support SHG makes them useful for frequency doubling, where incoming laser light is converted into higher harmonics. This capability is valuable in applications such as laser diagnostics, telecommunications, and precision measurement systems. One of their key advantages is their flexibility in composition and structure, which enables the design of custom optical materials tailored to specific needs. Moreover, the ability to incorporate different materials into their pores enhances their versatility. This allows the design of multifunctional materials that not only have NLO properties but also improve chemical stability or specific optical absorption characteristics. The SHG properties observed in the Zn(II) azo Schiff base complex, particularly when incorporated into a nanoporous $p\mathrm{SiO_2}$ matrix, suggest potential applications in NLO microscopy and sensor technologies. Given that SHG is frequently used in biomedical applications, our materials could also be explored for such uses with further experimental validation.

3. Conclusion

In summary, our study focused on the NLO properties of azo based Schiff base ligand and its corresponding complexes with Zn(II) and Cu(II) cations, highlighting the critical role of metal-ligand coordination in tuning their NLO behavior. The metal centers in these complexes contribute to enhanced electronic polarization, while π-conjugation enables efficient charge transfer. These processes directly influence their ability to exhibit strong NLO effects, such as self-focusing, 3rd order absorption, and 2nd order frequency doubling. The NLO investigations were divided into three parts based on the nature of the samples and the methodologies used. In the first phase, we evaluated the NLO refraction and NLO absorption of solutions using the Z-scan technique. These studies revealed a self-focusing effect and reversed saturable absorption in the examined samples. The $\mathrm{Zn(L)_2}$ complex demonstrated a higher 2PA than the $\mathrm{Cu(L)_2}$ complex, reflecting stronger electronic interactions from its fully filled d orbitals, which contribute to enhanced 3rd order NLO responses. In the second phase, we conducted 3rd order NLO studies on thin films created by spin coating, utilizing the THG via the Maker fringe method. Morphological characterization using optical microscopy and AFM demonstrated a high degree of homogeneity, with few defects and low surface roughness (RMS < 0.4 nm),

confirming that the films possess the optical quality needed for THG measurements. These results suggest that minor variations in film topography have a minimal impact on THG efficiency. The $Zn(L)_2$ complex showed the strongest THG response (21.76×10^{-22} m^2 V^{-2}) due to strong LMCT processes and electronic interactions in its d_{10} configuration. This complex exceeds previously studied transition-metal-based materials, highlighting its superior potential for photonic applications. The third phase focused on the SHG properties of the complex embedded within a nanoporous $pSiO_2$ membrane. The resulting hybrid nanocomposite, $pSiO_2$:$Zn(L)_2$, exhibited a pronounced SHG response without the need for symmetry-breaking techniques, such as corona poling. The polarization-dependent measurements of the SHG signal confirmed its suitability for polarization-sensitive applications, as the material demonstrated slight variation with polarization, effectively functioning as anisotropic medium. Unlike traditional SHG materials, these nanocomposites do not require phase matching or complex poling treatments, making them highly attractive for practical optical system implementations. Importantly, embedding the $Zn(L)_2$ complex within a nanoporous $pSiO_2$ membrane activated SHG in a material previously SHG-inactive in thin film form. This confinement-induced symmetry breaking and the resultant polarization-dependent anisotropy represent a novel mechanism distinct from traditional poling or crystalline alignment methods, marking a significant advancement in hybrid NLO materials. In conclusion, the azo Schiff base complexes studied here, particularly $Zn(L)_2$, exhibit strong NLO properties across both 3rd order and 2nd order effects. Our results highlight the importance of metal-ligand interactions and electronic structure in enhancing the NLO behavior and stability, which make them promising candidates for optoelectronic and photonic applications. The calculated nonlinear FOMs for all systems affirm their suitability for practical applications such as ultrafast all-optical switching and frequency conversion, bridging fundamental understanding with technological relevance. The versatility of the nanoporous membranes further enhances the applicability of these materials, enabling multifunctional designs tailored for specific NLO requirements and positioning these complexes as advantageous alternatives to conventional transition-metal-based materials.

4. Experimental Section

Thin Films Characterization: The surface properties of the thin films were examined using a Bioscope II AFM equipped with a Nanoscope V controller (Veeco). A PPP-NCST silicon cantilever (Nanosensors) was used to scan an area of ≈ 3 µm × 3 µm. The resulting AFM images were analyzed using Gwyddion 2.64 software,[66] providing detailed insights into the film profile and surface roughness. Linear optical parameters, including the refractive index (n) and extinction coefficient (k), were obtained through ellipsometry measurements (UVISEL Horiba Jobin Yvon) at specifically selected wavelengths: 1064 nm, which corresponds to the laser wavelength, and 355 nm, which corresponds to the wavelength of the THG. From these measurements, the real (ε') and imaginary (ε″) parts of the dielectric permittivity (ε) were calculated. These data facilitate the determination of NLO parameters using theoretical models. Additionally, the thickness of the guest-host films was measured using a profilometer (Dektak 6 M).

Absorption and Emission Spectroscopy: Optical absorption spectra of the thin films were recorded using a UV-1800 UV/VIS/NIR spectrometer (Shimadzu) over the wavelength of 1100 to 300 nm. PL spectra were measured with a FluoroMax-4 spectrofluorometer (Horiba), focusing on the maximum absorbance wavelengths and including PL intensity as a function of excitation and emission wavelengths. The PL lifetimes were subsequently recorded using the FluoroMax-4 spectrofluorometer combined with the Single Photon Counting Controller FluoroHub, employing a pulse diode with an excitation wavelength closely matched to that of the studied sample.

Z-Scan Technique: This method allows for the simultaneous measurement of both NLO refraction (Close Aperture Z-scan, CA) and NLO absorption (Open Aperture Z-scan, OA) within a single measurement.[67] An ultrafast Nd:YAG laser (Ekspla, PL2250 Series) was employed, with an output wavelength of 532 nm, a pulse duration of 30 ps, and a repetition rate of 10 Hz. The laser beam had a diameter of ≈ 17 µm, and the peak intensity was set to 23.49 GW cm^{-2} with a focal length of 20 cm. To minimize potential thermal nonlinear effects, the laser pulse duration and intensity were optimized to prevent thermal accumulation, making sure that the NLO effects were mainly electronic. No evidence of thermal asymmetries was observed during the measurements. The sample was translated along the z-axis from −15 to 15 mm, where the focal point is designated as 0, with a step 0.5 mm. The signals corresponding to NLO absorption and NLO refraction were recorded in one measurement.

THG and SHG: Additionally, to Z-scan measurements, 3rd order NLO phenomena were explored using the Maker fringe technique, which facilitates the measurement of THG.[68,69] During this process, the THG intensity was recorded while rotating the thin film sample from −60° to 60° with a step 0.5°. The Nd:YAG laser source (Ekspla, PL2250 Series), which operate at a wavelength of 1064 nm, with a pulse duration of 30 ps and repetition rate of 10 Hz, was employed. The laser beam had a diameter of ≈ 40 µm, with a peak intensity of 239 GW cm^{-2} and a focal length of 25 cm. Similarly to Z-scan, the laser intensity and pulse duration were selected to avoid significant thermal effects, making sure that the observed harmonics were driven by electronic nonlinearities rather than thermal processes. Polarization and energy of the laser beam were modulated using a half-wave plate and a Glan-Taylor polarizer, allowing control over the s-p and p-p polarizations. The THG signal was collected through a 355 nm filter and detected using a photomultiplier tube. Furthermore, by switching the filter to 532 nm, the SHG signal in nanocomposites was recorded while keeping all other parameters unchanged, like those used for THG.

Supporting Information

Supporting Information is available from the Wiley Online Library or from the author.

Acknowledgements

The presented results are part of a project that has received funding from the European Union's Horizon Europe research and innovation program under the Marie Skłodowska-Curie Grant agreement no. 101086493. A.V.K. acknowledges the project co-financed by the Polish Ministry of Education and Science under the program "Co-financed international projects", project no. W26/HE/2023 (Dec. MEiN 5451/HE/2023/2). Research in this paper were performed using Interdisciplinary Centre for Modern Technologies facilities, NCU, Toruń, Poland.

Conflict of Interest

The authors declare no conflict of interest.

Author Contributions

K.W. performed investigation, formal analysis, visualization, data curation, wrote the original draft, wrote reviewed and edited the final

manuscript. M.B. performed investigation, synthesis, resources, wrote reviewed and edited the final manuscript. S.S. performed synthesis and resources. A.A. performed synthesis and resources. A.E.G. performed methodology, resources, supervision, wrote reviewed and edited the final manuscript. J.S. performed methodology, investigation, resources. A.Z. performed methodology, resources. A.V.K. performed synthesis, methodology, acquired funding acquisition, wrote reviewed and edited the final manuscript. P.H. performed methodology, resources, wrote reviewed and edited the final manuscript. B.S. performed conceptualization, methodology, supervision, acquired funding acquisition, wrote reviewed and edited the final manuscript.

Data Availability Statement

The data that support the findings of this study are available from the corresponding author upon reasonable request.

Keywords

azo Schiff base, nanoporous membranes, second harmonic generation, third harmonic generation, z-scan

Received: March 28, 2025
Revised: August 20, 2025
Published online:

[1] S. Semin, X. Li, Y. Duan, T. Rasing, *Adv. Opt. Mater.* **2021**, *9*, 2100327.
[2] R. Shi, X. Han, J. Xu, X.-H. Bu, *Small* **2021**, *17*, 2006416.
[3] S.-S. Han, W.-D. Yao, S.-X. Yu, Y. Sun, A. Gong, S.-P. Guo, *Inorg. Chem.* **2021**, *60*, 3375.
[4] S.-J. Kim, B. J. Kang, U. Puc, W. T. Kim, M. Jazbinsek, F. Rotermund, O.-P. Kwon, *Adv. Opt. Mater.* **2021**, *9*, 2101019.
[5] Z. Dehghani, M. Nadafan, M. B. Mohammadzadeh Shamloo, Z. Shadrokh, S. Gholipour, M. H. Rajabi Manshadi, S. Darbari, Y. Abdi, *Optics Laser Technol.* **2022**, *155*, 108352.
[6] Z. Shadrokh, S. Sousani, Z. Dehghani, N. Kabir, A. Mozaffarbeigi, N. Mrkyvkova, A. Abbasi, Y. Abdi, P. Siffalovic, E. Majkova, M. Jergel, *Opt. Mater.* **2025**, *161*, 116771.
[7] Z. Bai, K. M. Ok, *Coord. Chem. Rev.* **2023**, *490*, 215212.
[8] S. Irshad, F. Ullah, S. Khan, R. Ludwig, T. Mahmood, K. Ayub, *Optics Laser Technol.* **2021**, *134*, 106570.
[9] J. Zhou, Q. Wu, A. Ji, Z. Jia, M. Xia, *Coord. Chem. Rev.* **2025**, *524*, 216332.
[10] J.-L. Zhou, L. Guo, W.-D. Yu, Z.-H. Zhang, Y. Wang, J. Yan, *Inorg. Chem. Commun.* **2019**, *99*, 189.
[11] N. Dege, Ö. Tamer, M. Şimşek, D. Avcı, M. Yaman, A. Başoğlu, Y. Atalay, *Appl. Organomet. Chem.* **2022**, *36*, 6678.
[12] F. Ullah, S. Irshad, S. Khan, M. A. Hashmi, R. Ludwig, T. Mahmood, K. Ayub, *J. Phys. Chem. Solids* **2021**, *151*, 109914.
[13] D. Avcı, Ö. Özge, F. Sönmez, A. Başoğlu, Ö. Tamer, Y. Atalay, *Mater. Sci. Semicond. Process.* **2024**, *179*, 108523.
[14] S. Kahraman, C. Hepokur, F. Erci, S. Erkan, S. Cetin, M. Kose, M. Kurtoglu, *Polyhedron* **2025**, *269*, 117393.
[15] A. Kakanejadifard, V. Khojasteh, A. Zabardasti, F. Azarbani, *Org. Chem. Res.* **2018**, *4*, 210.
[16] M. R. Abd-Alzahra, Z. M. Hatem, N. Q. A. Maged, I. K. Kareem, *Int. J. Health Sci.* **2022**, *6*, 5524.
[17] T. I. Mohammed, *Int. J. Pap. Adv. Sci. Rev.* **2023**, *4*, 42.
[18] H. Nakatori, T. Haraguchi, T. Akitsu, *Symmetry* **2018**, *10*, 147.
[19] B. Li, Y. Shi, Z. Fu, *J. Polym. Sci. A Polym. Chem.* **2019**, *57*, 1653.
[20] S. Kamali, M. Orojloo, R. Arabahmadi, S. Amani, *J. Photochem. Photobiol. A Chem.* **2022**, *433*, 114136.
[21] T. M. Shatir, K. A. Aly, M. M. Ebrahium, Y. B. Saddeek, E. R Kumar, *J. Mol. Liq.* **2024**, *401*, 124636.
[22] X. Yang, F. Zhu, W. Shi, Y. Li, Y. Zeng, M. Yan, Y. Cui, G. Sun, *Spectrochim. Acta A Mol. Biomol. Spectrosc.* **2020**, *226*, 117608.
[23] J. C. Qin, L. Fan, Z. Y. Yang, *Sensors Actuators B Chem* **2016**, *228*, 156.
[24] A. S. Burlov, V. G. Vlasenko, Yu. V. Koshchienko, N. I. Makarova, A. A. Zubenko, Y. D. Drobin, L. N. Fetisov, A. A. Kolodina, Y. V. Zubavichus, A. L. Trigub, S. I. Levchenkov, D. A. Garnovskii, *Polyhedron* **2018**, *154*, 65.
[25] S. Banerjee, A. Dey, P. Ghorai, P. Brandão, J. Ortega-Castro, A. Frontera, P. P. Ray, A. Saha, *New J. Chem.* **2018**, *42*, 13430.
[26] H. Zeng, K. Liang, L. Jiang, D. Zhao, B. Kong, *Acc. Chem. Res.* **2025**, *58*, 732.
[27] Z. Yuan, Z. Liang, L. Yang, D. Zhou, Z. He, J. Yang, C. Wang, L. Jiang, W. Guo, *ACS Nano* **2024**, *18*, 24581.
[28] Y. Ma, J. Kaczynski, C. Ranacher, A. Roshanghias, M. Zauner, B. Abasahl, *Microelectron. Eng.* **2018**, *198*, 29.
[29] X. Wang, X. Liu, Z. Li, H. Zhang, Z. Yang, H. Zhou, T. Fan, *Adv. Funct. Mater.* **2020**, *30*, 1907562.
[30] Y. Guo, C. Qian, Y. Wu, J. Liu, X. Zhang, D. Wang, Y. Zhao, *J. Energy Chem.* **2021**, *63*, 74.
[31] L. N. Fernandez Solis, G. J. Silva Junior, M. Bertotti, L. Angnes, S. V. Pereira, M. A. Fernández-Baldo, M. Regiart, *Talanta* **2024**, *273*, 125971.
[32] B. Graczykowski, A. El Sachat, J. S. Reparaz, M. Sledzinska, M. R. Wagner, E. Chavez-Angel, Y. Wu, S. Volz, F. Alzina, C. M. Sotomayor Torres, *Nat. Commun.* **2017**, *8*, 415.
[33] A. Shiohara, B. Prieto-Simona, N. H. Voelcker, *J. Mater. Chem. B* **2021**, *9*, 2129.
[34] N. Gostkowska-Lekner, D. Kojda, J.-E. Hoffmann, M. May, P. Huber, K. Habicht, T. Hofmann, *Microporous Mesoporous Mater.* **2022**, *343*, 112155.
[35] J. Kusz, C. Boissiere, Y. Bretonnière, C. Sanchez, S. Parola, *Nanoscale* **2024**, *16*, 18918.
[36] K. Waszkowska, P. Josse, C. Cabanetos, P. Blanchard, B. Sahraoui, D. Guichaoua, I. Syvorotka, O. Kityk, R. Wielgosz, P. Huber, A. V. Kityk, *Opt. Lett.* **2021**, *46*, 845.
[37] Y. Shchur, H. El Karout, B. Sahraoui, A. Andrushchak, G. Beltramo, D. Pustovyi, S. Vitusevich, P. Huber, A. V. Kityk, *Sci. Rep.* **2024**, *14*, 24237.
[38] J. Xiao, M. Cong, M. Li, X. Zhang, Y. Zhang, X. Zhao, W. Lu, Z. Guo, X. Liang, G. Qing, *Adv. Funct. Mater.* **2024**, *34*, 2307996.
[39] W. K. Kipnusu, C. Doñate-Buendía, M. Fernández-Alonso, J. Lancis, G. Mínguez-Vega, *Part. Part. Syst. Charact.* **2020**, *37*, 2000093.
[40] Y. Shchur, A. V. Kityk, V. V. Strelchuk, A. S. Nikolenko, N. A. Andrushchak, P. Huber, A. S. Andrushchak, *J. Alloys Compd.* **2021**, *868*, 159177.
[41] K. Waszkowska, Y. Cheret, D. Guichaoua, T. Travers, A. El-Ghayoury, D. Gindre, P. Göring, M. Lelonek, A. Andrushchak, I. Goncharova, B. Sahraoui, *Opt. Lett.* **2023**, *48*, 2897.
[42] J. Huang, Y. Zhang, J. Guo, Z. Yang, Y. Bai, G. Gao, J. Zhu, B. B. Mamba, H. Wang, L. Shao, *J. Membr. Sci.* **2024**, *711*, 123216.
[43] X. Huang, S. Cheng, C. Huang, J. Han, M. Li, S. Liu, J. Zhang, P. Zhang, Y. You, W. Chen, *Small* **2024**, *20*, 2311219.
[44] N. Hampu, M. A. Hillmyer, *ACS Appl. Polym. Mater.* **2019**, *1*, 1148.
[45] M. L. Pereira Júnior, L. A. Ribeiro Júnior, *FlatChem* **2020**, *24*, 100196.
[46] S. Slassi, A. El-Ghayoury, M. Aarjane, K. Yamni, A. Amine, *Appl. Organomet. Chem.* **2020**, *34*, 5503.
[47] G. Beadie, M. Brindza, R. A. Flynn, A. Rosenberg, J. S. Shirk, *Appl. Opt.* **2015**, *54*, F139.
[48] A. Zawadzka, P. Płóciennik, A. Korcala, P. Szroeder, *Opt. Mater.* **2019**, *96*, 109295.

[49] K. Iliopoulos, D. Potamianos, E. Kakkava, P. Aloukos, I. Orfanos, S. Couris, *Opt. Express* **2015**, *23*, 24171.
[50] M. R. Ferdinandus, M. Reichert, T. R. Ensley, H. Hu, D. A. Fishman, S. Webster, D. J. Hagan, E. W. Van Stryland, *Opt. Mater. Express* **2012**, *2*, 1776.
[51] A. Zakery, S. R. Elliott, *Optical Nonlinearities in Chalcogenide Glasses and their Applications*, Springer, Berlin, New York **2007**.
[52] R. W. Boyd, *Nonlinear Optics*, 3rd ed, Academic Press, Cambridge, Massachusetts **2003**.
[53] B. Kulyk, D. Guichaoua, A. Ayadi, A. El-Ghayoury, B. Sahraoui, *Dyes Pigm.* **2017**, *145*, 256.
[54] S. Taboukhat, N. Kichou, J.-L. Fillaut, O. Alévêque, K. Waszkowska, A. Zawadzka, A. El-Ghayoury, A. Migalska-Zalas, B. Sahraoui, *Sci. Rep.* **2020**, *10*, 15292.
[55] H. Belahlou, A. Karakas, K. Waszkowska, A. Gozutok, M. Karakaya, M. Guergouri, A. Bouraiou, S. Bouacida, B. Sahraoui, K. Bouchouit, *Cryst. Growth Des.* **2023**, *23*, 6331.
[56] K. Waszkowska, Y. Cheret, A. Ayadi, A. Zawadzka, J. Strzelecki, A. El-Ghayoury, A. V. Kityk, A. Andrushchak, B. Sahraoui, *J. Mol. Struct.* **2024**, *1307*, 137912.
[57] M. Wakaki, *Optical Materials and Applications*, 1st ed., CRC Press, Boca Raton, FL, USA **2013**.
[58] R. A. Myers, N. Mukherjee, S. R. J. Brueck, *Opt. Lett.* **1991**, *16*, 1732.
[59] T. Verbiest, K. Clays, V. Rodriguez, *Second-order Nonlinear Optical Characterization Techniques: An Introduction*, CRC Press, Boca Raton, FL, USA **2009**, pp. 92-93.
[60] F. Kajzar, Y. Okada-Shudo, C. Meritt, Z. Kafafi, *Synth. Met.* **2001**, *117*, 189.
[61] G. D. Boyd, R. C. Miller, K. Nassau, W. L. Bond, A. Savage, *Appl. Phys. Lett.* **1964**, *5*, 234.
[62] T. A. Driscoll, H. J. Hoffman, R. E. Stone, P. E. Perkins, *J. Opt. Soc. Am. B* **1986**, *3*, 683.
[63] R. Loucif-Saibi, K. Nakatani, J. A. Delaire, M. Dumont, Z. Sekkat, *Chem. Mater.* **1993**, *5*, 229.
[64] A. Dhinojwala, G. K. Wong, J. M. Torkelson, *J. Chem. Phys.* **1994**, *100*, 6046.
[65] P. E. Ohno, S. A. Saslow, H. Wang, F. M. Geiger, K. B. Eisenthal, *Nat. Commun.* **2016**, *7*, 13587.
[66] D. Nečas, P. Klapetek, *Open Phys.* **2012**, *10*, 181.
[67] M. Sheik-Bahae, A. A. Said, T. H. Wei, Y. Y. Wu, D. J. Hagan, M. J. Soileau, E. W. Van Stryland, Proceeding SPIE Nonlinear Optical Properties of Materials, SPIE, Bellingham, WA **1990**, pp. 1148.
[68] P. D. Maker, R. W. Terhune, M. Nisenoff, C. M. Savage, *Phys. Rev. Lett.* **1962**, *8*, 21.
[69] A. Szukalski, B. Sahraoui, B. Kulyk, C. A. Lazar, A. M. Manea, J. Mysliwiec, *RSC Adv.* **2017**, *7*, 9941.